Earth and Planetary Science Letters xxx (xxxx) 119829

Contents lists available at ScienceDirect

Earth and Planetary Science Letters

journal homepage: www.elsevier.com

Journal logo

Trace element and stable Sr isotope evidence for seamount-driven variations in subducted sediment and carbon recycling in Central America

Alexander J. Hammerstrom [a, b, *], Rita Parai [c], Richard W. Carlson [d], Vlad C. Manea [e], Marina Manea [e], Stephen J. Turner [a, b]

[a] Department of Earth, Geographic, and Climate Sciences, University of Massachusetts Amherst, 233 Morrill 2627N. Pleasant St, Amherst 01003-9354, MA, USA
[b] Department Geology and Geophysics, Woods Hole Oceanographic Institution, 266 Woods Hole Road, Woods Hole 02543-1050, MA, USA
[c] Department of Earth and Planetary Sciences, Washington University in St. Louis, 1 Brookings Drive, St. Louis 63130, MO, USA
[d] Earth and Planets Laboratory, Carnegie Institution for Science, 5241 Broad Branch Rd. NW, Washington, DC, 20015, USA
[e] Computational Geodynamics Laboratory, Instituto de Geociencias, Universidad Nacional Autonoma de Mexico, Campus Juriquilla, Queretaro, 76230, Mexico

ARTICLE INFO

Editor: Dr Fang-Zhen Teng

Keywords:
Sr isotopes
Subduction
Arc geochemistry
Central America
Carbonate recycling
Seamounts

ABSTRACT

Subduction zone fluxes control the long-term evolution of Earth's interior, surface reservoirs, and climate. To better constrain these fluxes, we present new $\delta^{88}Sr$ measurements of lavas and sediments from Nicaragua, a key site of carbonate subduction. $\delta^{88}Sr$ data are interpreted alongside existing trace element data to assess the value of Sr stable isotopes as a quantitative subduction tracer. Trace element systematics (1) constrain ambient mantle enrichment and extent of melting (Nb vs. Yb), (2) show that the arc's Sr budget is dominated by melts of subducting altered ocean crust (AOC) (Yb/Sr vs. $^{87}Sr/^{86}Sr$), and (3) verify that incompatible element compositions are controlled by variable recycling of hemipelagic vs. carbonate sediments (Th/Sr vs. $^{87}Sr/^{86}Sr$). Other trace element ratios, such as Nd/Sr, require varying AOC melt compositions. A full forward trace element model confirms the viability of this interpretation. The new $\delta^{88}Sr$ data build on and corroborate these findings. The range of $\delta^{88}Sr$ in arc lavas cannot be explained by sediment proportions or ambient mantle compositions, but instead requires $\delta^{88}Sr$ heterogeneity in the subducting oceanic crust. Notably, AOC $\delta^{88}Sr$ appears to co-vary with the proportion of hemipelagic vs. carbonate sediment recycled to the arc. We suggest these variations reflect seamount subduction, where seamounts with heterogeneous $\delta^{88}Sr$, emplaced during the transition in marine sediment deposition, cap carbonate layers and control their transfer to the arc. Within this framework, we estimate 45% to 60% of subducted carbonate-derived carbon is returned to the arc, consistent with volcanic gas–based estimates.

1. Introduction

Subduction zones are major pathways for geochemical exchange between Earth's surface and interior, playing a central role in continental crust generation and global volatile cycling. Understanding the fate of subducted carbon is particularly important for constraining Earth's long-term evolution and climate stability (Dasgupta and Hirschmann, 2010; Sleep and Zahnle, 2001). Direct measurements of magmatic CO_2 fluxes are challenging, however, due to extensive deep-crustal degassing, leading to reliance on indirect volcanic gas proxies (Barry et al., 2019; de Moor et al., 2017; Freundt et al., 2014; Shaw et al., 2003). These methods have limitations because volcanic CO_2 fluxes vary spatially and temporally and processes like diffuse degassing remain poorly constrained (e.g., de Moor et al., 2017). Additionally, carbon isotopes can fractionate during slab devolatilization, crustal contamination, and shallow processes in the forearc (Barry et al., 2019; Plank and Manning, 2019). Current estimates of carbon recycling at arc volcanoes range from 14% to 100% (Barry et al., 2019; Dasgupta and Hirschmann, 2010; de Moor et al., 2017; Freundt et al., 2014; Kelemen and Manning, 2015; Shaw et al., 2003), underscoring the need for more robust geochemical proxies that can trace slab-derived CO_2.

Here, we re-examine the geochemical variability among lavas from the Central American Arc (Fig. 1a), a key location for understanding carbonate subduction on the modern Earth, as well as an important case study to address the controls on key trace element tracers of slab materials. Central America, Nicaragua in particular, is ideal for this study

* Corresponding author.
E-mail addresses: ahammerstrom@whoi.edu, ahammerstrom@umass.edu (A.J. Hammerstrom), parai@wustl.edu (R. Parai), rcarlson@carnegiescience.edu (R.W. Carlson), vlad@geociencias.unam.mx (V.C. Manea), marina@geociencias.unam.mx (M. Manea), stephen.turner@whoi.edu (S.J. Turner).

https://doi.org/10.1016/j.epsl.2026.119829
Received 12 September 2025; Received in revised form 24 December 2025; Accepted 5 January 2026
0012-821/

due to a large flux of subducting marine carbonate sediments which has been linked to high CO_2 fluxes from the arc (Barry et al., 2019). Lavas from Central America also exhibit correlations among geochemical indices that contradict their usual interpretation as 'fluid' vs 'melt' tracers and may instead serve as crucial constraints on the recycling efficiency of sediments (i.e., the proportion of subducted sediment that is recycled to the arc) with varying carbonate abundances (Fig. 2; Patino et al., 2000). We also assess the potential of stable strontium isotope ratios (δ^{88}Sr) as a novel tracer of subduction processes, specifically carbonate subduction.

We find that variable recycling efficiencies of different layers of subducting sediment, rather than ocean crust fluids, are the dominant control on most incompatible trace element abundances in Central American arc lavas, confirming the interpretation of Patino et al. (2000). In addition, sediment recycling efficiency co-varies with the δ^{88}Sr composition of the subducting mafic ocean crust and the relative flux of Sr vs less mobile trace elements from the slab to the arc. We propose that subducting seamounts can account for these co-variations, and show that this general geochemical framework can be used to produce unique constraints on the fate of subducting carbon.

2. Background

2.1. Nicaraguan arc volcanism

The Nicaraguan arc segment lies in the middle of the Central American Arc, which extends ~1400 km from the Mexico-Guatemala border to Panama (Fig. 1a). The upper plate of the Nicaraguan segment is thin and mostly oceanic with little evidence for crustal assimilation by ascending magmas (Reagan et al., 1994). The subducting Cocos plate consists of 24 Ma ocean crust, formed at the East Pacific Rise, overlain by a lower layer of ~200 m of carbonate-rich sediment (Figs. 1c-d) and an

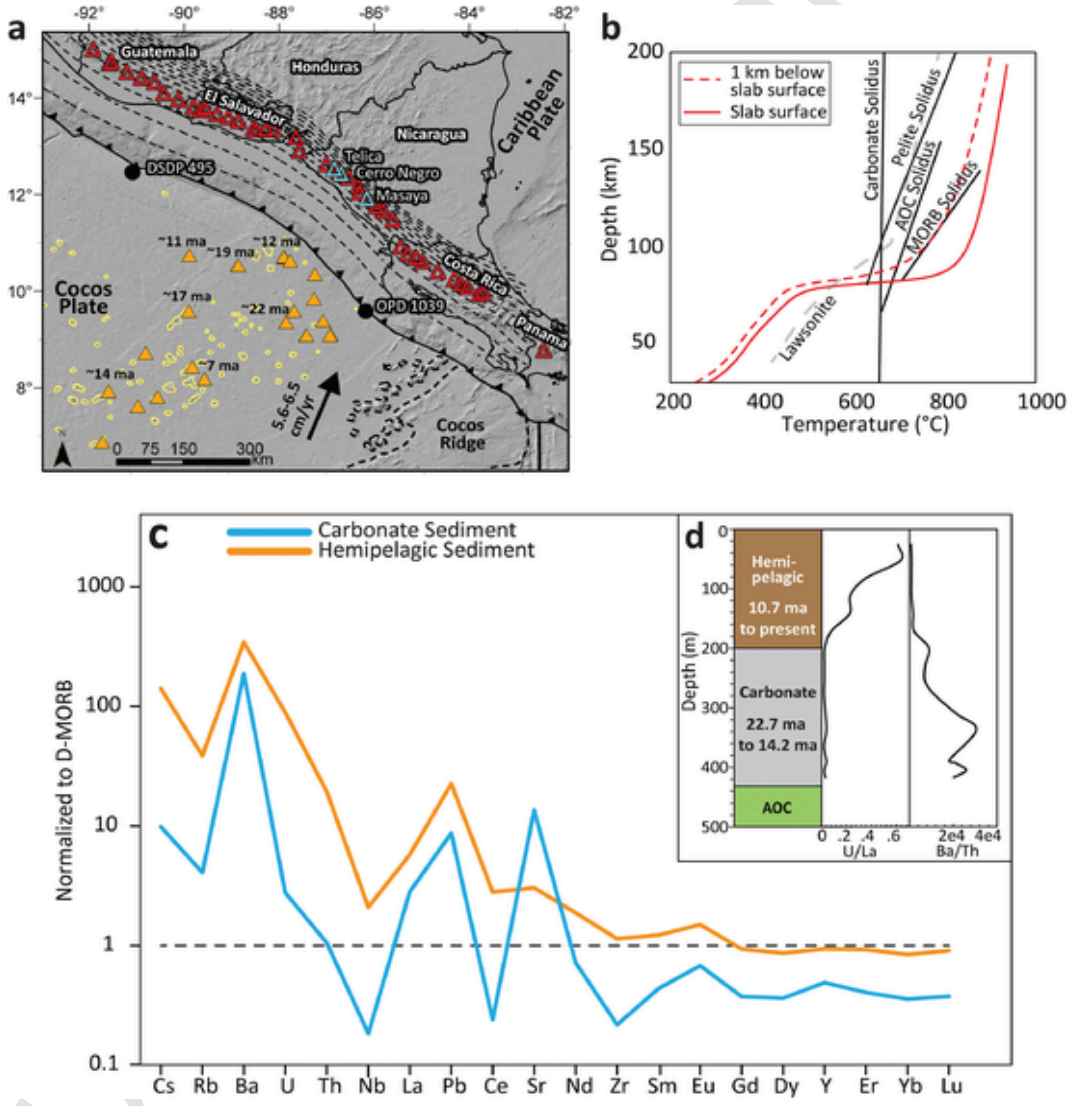

Fig. 1. Background information about the study region, slab thermal conditions, and subducting sediment units. (a) Map of Central American Arc. Open red triangles are arc front volcanoes, open blue triangles are volcanoes analyzed in this study. Cocos plate seamounts are outlined in yellow, solid orange triangles are seamounts sampled (and in some cases dated) by Herbrich et al. (2015). Thin black dashed lines are depth to slab surface contours (CI = 20 km) from Hayes et al. (2018). **(b)** Slab thermal profiles at the surface (solid red line) and 1 km below the slab surface as compared to the H_2O-saturated solidus for carbonate (Wyllie and Boettcher, 1969), pelitic sediments (Hermann and Spandler, 2008), AOC (Spandler and Pirard, 2013), and MORB (Sisson and Kelemen, 2018). The slab thermal profiles are the farbi = 2 model of van Keken et al. (2018), designed to emulate a moderate amount of shear heating. **(c)** Incompatible element diagram of average carbonate and hemipelagic sediment compositions from DSDP 495 (see panel a) from Patino et al. (2000) normalized to DMORB (Gale et al. 2013). **(d)** General stratigraphy of DSDP site 495 with U/La and Ba/Th ratios vs depth. One sample with an anomalously high Ba/Th was omitted to preserve scale.

upper layer of ~200 m of hemipelagic sediment (Aubouin and Von Huene, 1982). The oceanic plate also carries numerous seamounts up to 2 km high and 14 km wide (Fig. 1a; Herbrich et al., 2015). A comparison between thermo-mechanical models and experimentally determined solidus temperatures (see Fig. 1b) indicates that at least the upper 1 km of the slab reaches temperatures that exceed the H_2O-saturated solidi for carbonate/pelitic sediments and mafic ocean crust. Progressive lawsonite dehydration in the lower slab layers occurs at temperatures 100–200°C below the slab solidi, providing a fluid flux to the overriding layers (Turner et al., 2023). This supports hydrous slab melting as the dominant process by which subducting materials are transferred from the slab to the mantle wedge.

Nicaraguan arc lava geochemistry is notably diverse, with compositions that appear to reflect varying contributions from subducting sediments. The effect of the differing subducted sediments on the arc is apparent from the negative correlation between Ba/Th and U/La (Fig. 2). These ratios distinguish between hemipelagic and carbonate sediment because the carbonate layer is diluted in most trace elements aside from Sr, Ba, La, and Pb (Fig. 1c), leading to distinctly low U/La and high Ba/Th (Fig. 1d). Though ratios such as these are sometimes interpreted as 'aqueous fluid' proxies (Elliott, 2004), fluid-dominated transport would have instead resulted in a positive correlation on Fig. 2, as U and Ba partition preferentially into fluids relative to La and Th. Sediment-driven variability is also supported by a positive correlation between U/La and $^{10}Be/^{9}Be$ and general mass-balance considerations (Reagan et al., 1994; Turner and Langmuir, 2024). Despite the relatively constant thickness of offshore sediment layers, the sediment composition expressed in arc magmas is highly variable, a discrepancy that remains unresolved. Patino et al. (2000) hypothesized that this could be due either to off-scraping of the upper hemipelagic sediments from horsts to grabens, or a more complicated multi-stage slab melting process.

While trace element geochemistry has shed substantial light on the origins of Central American arc lavas, the U/La and Ba/Th proxies do not provide direct quantitative constraints on sediment recycling efficiency. For U/La, this is because U decreases significantly downcore within the hemipelagic layer as the proportion of preserved organic-rich sediment decreases (Fig. 1d; Patino et al., 2000; Plank et al., 2002). The relationship between Ba/Th in sediments vs lavas is impacted by the loss of sedimentary Ba by barite dissolution beneath the accretionary prism (Peccia et al., 2025; Solomon and Kastner, 2012). These complications motivate the development of additional tracers of sediment (and therefore carbon) recycling efficiency.

2.2. Strontium stable isotopes as a geochemical tracer

Strontium stable isotopes (reported as $^{88}Sr/^{86}Sr$ in standard delta notation, relative to NIST SRM-987 in units of permil as: $\delta^{88}Sr$ (‰) = $[(^{88}Sr/^{86}Sr)_e/(^{88}Sr/^{86}Sr)_{SRM987} - 1] \times 1000$) have the potential to serve as a tool to track carbonate subduction. Sr^{2+} readily substitutes for Ca^{2+}, leading to elevated Sr abundances in most carbonate-rich marine sediments. Seawater ($\delta^{88}Sr$ = 0.39‰, Fig. 3; Krabbenhöft et al., 2010; Pearce et al., 2015) is enriched in heavy Sr isotopes by removal of light Sr by marine carbonate, with an average $\Delta^{88/86}Sr$ carbonate-seawater fractionation factor of -0.24‰ (Vollstaedt et al., 2014). High-temperature magmatic processes have little effect on Sr isotope fractionation in systems for which Sr behaves as an incompatible element. Plagioclase fractionation may have a small impact on magmatic $\delta^{88}Sr$ (Amsellem et al., 2018), though this can be mitigated by careful sample screening. Double-spike, thermal ionization mass spectrometry (TIMS) $\delta^{88}Sr$ measurements of MORB (n = 5) thus far range from 0.25‰ to 0.30‰ (Fig. 3; Klaver et al., 2020). Experimental work shows that high-temperature hydrothermal alteration of basalt leads to elevated $\delta^{88}Sr$ (Voigt et al., 2018), and while actual altered ocean crust (AOC) $\delta^{88}Sr$ measurements are also limited, existing data support this general process (Klaver et al., 2020). Together, these studies show that subducting materials, marine carbonates in particular, exhibit distinct $\delta^{88}Sr$ compositions that may be reflected as recycled components in mafic arc lavas.

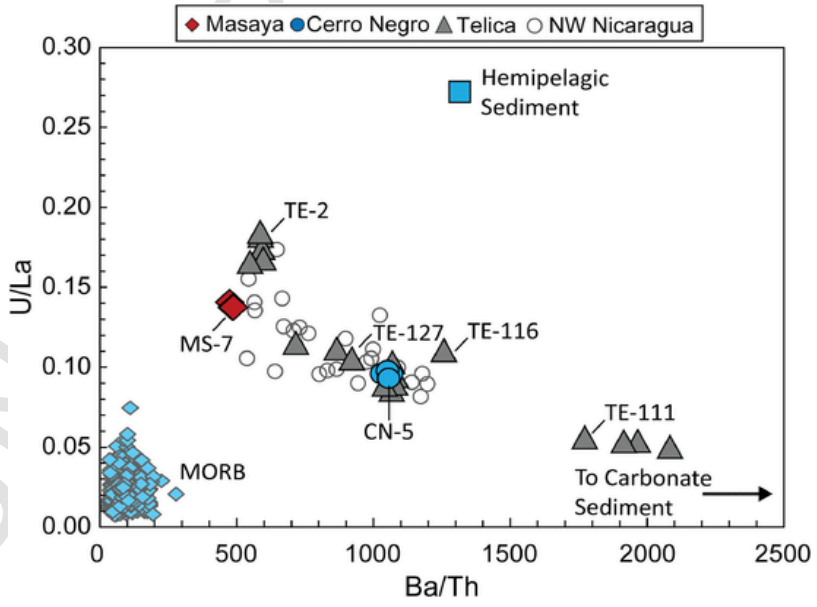

Fig. 2. Correlated U/La vs Ba/Th in lavas from NW Nicaragua demonstrates the influence of subducted hemipelagic vs carbonate sediment. Cerro Negro (filled blue circles) and Masaya (filled red diamonds) represent end member compositions while Telica lavas (grey filled triangles) span the full compositional range of NW Nicaraguan arc lavas (open grey circles). Plotted arc lavas include only 'Quality 35' data from Carr et al., (2014) with >3 wt.% MgO. Anomalous 'high Nb' (>3 ppm Nb) lavas are excluded, following Bolge et al. (2009). MORB are Mid-Atlantic Ridge data from Gale et al. (2013).

3. Samples and methods

3.1. Sample selection

Samples targeted for this study include six Nicaraguan arc lavas that have been previously characterized for major-element, trace-element, and radiogenic isotope compositions and three Cocos plate sediment samples from DSDP site 495 previously reported by Turner et al. (2023). The Nicaraguan Arc was selected based on a regional maximum in the recycled sediment signature, limited influence from crustal assimilation, and a normal depleted ambient mantle composition (i.e., the mantle prior to any slab contributions) that is not impacted by the Galapagos plume or enriched sub-continental lithospheric mantle (Bekaert et al., 2021; Heydolph et al., 2012). Well-characterized lavas were selected from Carr et al. (2014) from Cerro Negro, Masaya, and Telica volcanoes to encompass the full regional range of U/La and Ba/Th (Fig. 2). Only samples with Eu* >0.95 ($Eu/Eu^* = Eu_{cn}/[Sm_{cn} * Gd_{cn}]^{1/2}$) were included to minimize the influence of plagioclase fractionation. Cerro Negro and Masaya volcanoes represent distinct compositional end members in U/La vs Ba/Th space (Fig. 2) with limited intra-volcano variability in parental magma compositions (e.g., Zurek et al., 2019; Walker and Carr, 1986). As such, we have chosen the highest MgO sample available to represent each of these volcanoes. Multiple samples were measured from Telica, where erupted lavas span the full range of trace element variation exhibited in Nicaragua (Fig. 2). Four well-characterized arc lavas from the Chilean Southern Volcanic Zone (Turner et al., 2016, 2017) were also measured to enable a regional comparison to a convergent margin with more homogenous and predominantly terrigenous subducting sediment. The geologic reference standard JB-2 from Oshima (a basalt from the Izu Arc), and two AOC composite powders from ODP 801C (Kelley et al., 2003) previously measured for $\delta^{88}Sr$ by Klaver et al. (2020) were also analyzed.

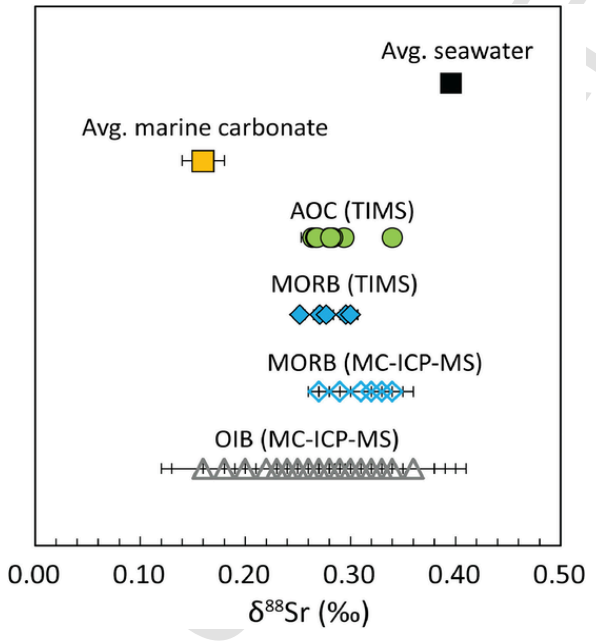

Fig. 3. Comparison of $\delta^{88}Sr$ literature data from select sources. Seawater from Krabbenhöft et al., (2010). Average marine carbonate following Pearce et al., 2015. AOC (TIMS) and MORB (TIMS) from Klaver et al. (2020). MORB (MC-ICP-MS) and OIB (MC-ICP-MS) from Amsellem et al. (2018). Amsellem et al. (2018) also reported several much higher $\delta^{88}Sr$ OIB samples they suggest have been affected by secondary alteration, which are omitted from this figure.

3.2. Thermal ionization mass spectrometry

Strontium isotope analyses were conducted via double-spike TIMS. Sample digestion and column chemistry were performed at the University of Massachusetts Amherst. Spiked and unspiked aliquots were digested in a 4:1 solution of 16 N Aristar Plus trace metal analysis grade HNO_3 and 48 N ultra-pure HF in Savillex beakers at 150°C for 48 hours, evaporated to dryness at 100°C, then dissolved and dried twice more using 20 ml of 16 N HNO_3. Following the second dry down, samples were re-digested in 1.5 ml of 8 N Aristar Plus trace metal analysis grade HNO_3 for 24 hr at 120°C. Reagent strength was calibrated to ensure separation of both Rb and Ba during column separation using Eichrom Sr-Spec resin, as incomplete Ba separation can lead to unpredictable mass discrimination during analysis (Scher et al., 2014). Purified samples were measured using a Thermo Scientific Triton TIMS at the Carnegie Institution for Science Earth and Planets Laboratory (for additional details see S1 and S2).

4. Results

$^{87}Sr/^{86}Sr$ and $\delta^{88}Sr$ data are presented in Table 1 and shown in Fig. 4 alongside existing Sr isotope TIMS measurements from AOC, MORB, and other arc lavas. The internal measurement precision (2-SE) is generally <0.01‰, though total measurement uncertainty is likely slightly larger (see S1). The AOC $\delta^{88}Sr$ measurements are consistent with measurements of the same samples by Klaver et al. (2020). Nicaraguan arc lava $\delta^{88}Sr$ measurements range from 0.212‰ to 0.322‰. Cerro Negro falls above the fields defined by currently available TIMS measurements of MORB and AOC (Fig. 4). Masaya, by contrast, falls below the field of AOC compositions and all other arc lavas, while Telica varies between them. The Chilean samples are much less variable, with $\delta^{88}Sr$ from 0.252‰ to 0.274‰. Carbonate sediment $\delta^{88}Sr$ ranges from 0.171‰ to 0.219‰, consistent with the calcareous Aegean sediments measured by Klaver et al. (2020). Surprisingly, the hemipelagic sediment sample has lower $\delta^{88}Sr$ (0.153‰) than the carbonate, likely reflecting the fact that a significant proportion of Sr in the hemipelagic sediment comes from iso-

Table 1
Sr isotope compositions via double-spike TIMS

Sample ID	Volcano/ Sample type	$\delta^{88}Sr$	2-SE	$^{87}Sr/^{86}Sr$	2-SE
Nicaraguan Arc					
CN-5	Cerro Negro	0.322	0.009	0.704071	0.000003
MS-7	Masaya	0.219	0.009	0.704187	0.000003
TE-2	Telica	0.260	0.009	0.704091	0.000003
TE-116	Telica	0.269	0.019	0.704139	0.000007
TE-127	Telica	0.243	0.009	0.704021	0.000003
TE-111	Telica	0.279	0.012	0.704001	0.000004
Chilean Arc					
DARE-160-CB	Antillanca	0.265	0.004	0.704138	0.000001
ANT14	Antuco	0.250	0.009	0.703952	0.000003
OSO23	Osorno	0.274	0.008	0.704388	0.000003
VILL13	Villarica	0.252	0.006	0.704084	0.000002
Izu Arc					
JB-2 (Reference Material)	Oshima	0.312	0.003	0.703751	0.000001
Cocos Plate Sediment					
495–12R3–20–21	Hemipelagic	0.153	0.007	0.707589	0.000002
495–24R4–20–21	Carbonate	0.171	0.009	0.708807	0.000003
495–37R4–20–21	Carbonate	0.219	0.007	0.708489	0.000003
AOC Composite Samples					
801C-MORB–110–220-FLO	Less altered	0.247	0.007	0.703301	0.000002
801C-MORB–110–220-VCL	Highly altered	0.263	0.009	0.706788	0.000003

Uncertainty is 2-SE measurement precision
Nicaraguan samples as reported in Carr et al. (2014) and citations therein
Chilean samples as reported in Turner et al. (2016, 2017)
Sediments from DSDP site 495, provided by request to IODP, also reported in Turner et al. (2023)
AOC samples as reported in Kelley et al. (2003)

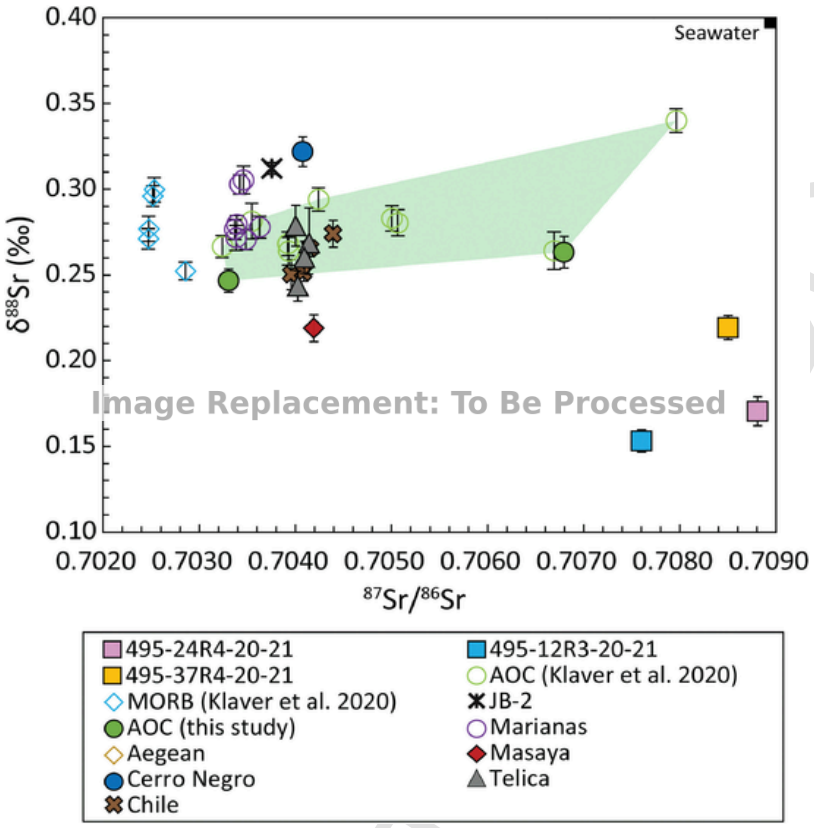

Fig. 4. $\delta^{88}Sr$ vs $^{87}Sr/^{86}Sr$ diagram of lavas and sediments from this study and Klaver et al. (2020)**.** Compared to lavas from MORB, Chile, and the Marianas, Nicaraguan arc lavas vary significantly in $\delta^{88}Sr$ over a narrow range of $^{87}Sr/^{86}Sr$. Samples from Cerro Negro, the Marianas Arc, and JB-2 (from Izu) plot above the array defined by variably altered MORB from ODP 801C (green shaded region), whereas Masaya plots below the array. Klaver et al. (2020) samples from Nisyros are omitted as their geochemistry is likely influenced by a slab tear and plagioclase fractionation (Klaver et al., 2016; Klaver et al., 2017).

topically light barite (Paytan et al., 2021). For example, given a terrigenous Ba/Al baseline of 0.005 (Dymond, 1992) and Ba and Al abundances measured in analogous core samples by Patino et al. (2000), barite would account for ~20% of the total Sr budget. Assuming $[Sr]_{barite} \approx 10{,}000$ ppm (Averyt et al., 2003), $\delta^{88}Sr_{barite} \approx -0.22‰$ (Paytan et al., 2021), and $\delta^{88}Sr_{terrigenous} = 0.27‰$ (BSE from Amsellem et al., 2018), predicts a $\delta^{88}Sr_{hemipelagic}$ of 0.17‰, which is close to the measured value. As a result, the Cocos Plate sediments have a smaller total range of $\delta^{88}Sr$ than the Nicaraguan arc lavas, with lower average $\delta^{88}Sr$.

5. Discussion

5.1. Re-evaluating melting processes and Sr sources via trace elements and $^{87}Sr/^{86}Sr$

To assess subduction fluxes across Nicaragua, we first constrain the ambient mantle wedge composition and degree of melting (F), which exert first-order controls on arc geochemistry (Turner and Langmuir, 2022a, 2022c). Elements like Nb and Yb (Fig. 5a) are useful for this because they are less affected by slab overprinting and have different sensitivities to ambient mantle enrichment and F. The gray and brown fields on Fig. 5a depict Yb and Nb concentrations calculated via non-modal batch melting at varying F based on depleted (blue swath) and enriched (brown swath) ambient mantle sources with 5% to 10% added slab melt (based on Turner and Langmuir, 2022b). Raw data for individual samples are plotted as solid symbols, and open symbols show estimated primary magma compositions based on the highest MgO sample from each volcanic edifice (see figure caption and S4 for additional details). The primary magma compositions are most consistent with 18% to 24% melting of a depleted mantle source. A subset of Nicaraguan samples are enriched in Nb and other high field strength elements (Bolge et al., 2009; Heydolph et al., 2012) possibly due to transient enrichment of the ambient mantle. The yellow triangles in Fig. 5a represent Telica lavas erupted from satellite cones and are depleted in Nb relative to main vent lavas (gray triangles). While these high-Nb samples and monogenetic cones are interesting, they are not representative of a significant volume of the arc and are not included in this study.

The Yb/Sr vs $^{87}Sr/^{86}Sr$ diagram in Fig. 5b can help to distinguish between slab (sediment and mafic ocean crust) and ambient mantle contributions to the arc, because melts of subducting ocean crust and sediment both have much lower Yb/Sr than the ambient mantle, but very different $^{87}Sr/^{86}Sr$. As shown on Fig. 5b, adding AOC melt to the ambient mantle will rapidly decrease Yb/Sr. Sediment melt will also reduce Yb/Sr, but will rapidly increase $^{87}Sr/^{86}Sr$. The arc lavas on Fig. 5b lie much closer to the ambient mantle-AOC melt mixing line than they do to the sediment, which means that the bulk slab melt must be dominated by Sr from the mafic ocean crust and that Yb/Sr is predominantly controlled by AOC melt addition. The gray field outlines the range of mixing trajectories consistent with the arc compositions. At the points of intersection between the gray field and the ambient mantle-AOC melt mixing line, the ambient mantle can contribute only 9% to 14% of the Sr to the arc. To reach the $^{87}Sr/^{86}Sr$ of the arc lavas, approximately 2% sediment melt must be added (though this value is better constrained by sediment-dominated elements such as Th, as discussed below), indicating that sediment contributes ~23% of the total Sr to the arc. These considerations confirm that the Sr budget of the arc is dominated by AOC melt.

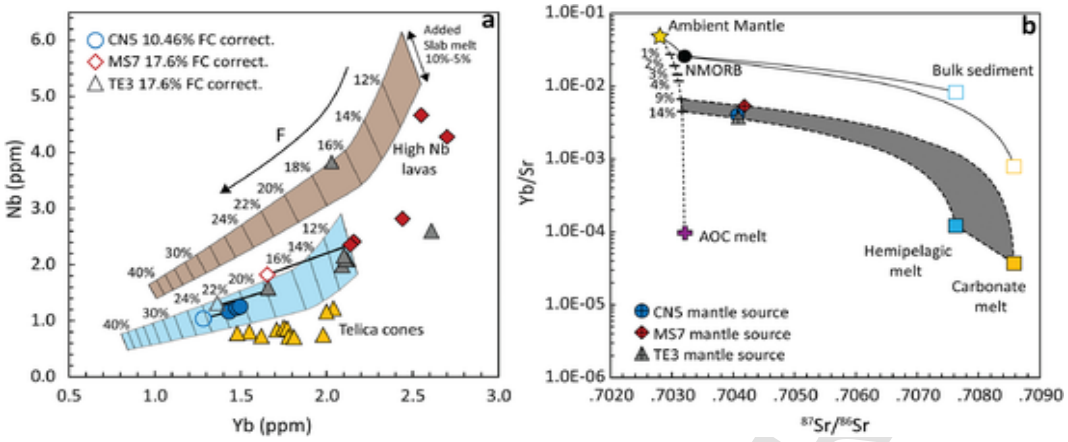

Fig. 5. Trace element and isotope systematics provide initial constraints on extents of melting and slab contributions to Nicaraguan lavas. (a) Melting curves are projected over Nicaraguan arc lava data on a plot of Yb vs Nb to assess ambient mantle composition and extent of mantle melting (F). The dotted lines correspond to varying F, in 2% intervals, using a non-modal melting model (see S3 and S4). The blue swath shows varying F from a depleted ambient mantle composition, the brown swath is based on an enriched (OIB-like) composition (Turner and Langmuir, 2022c). The widths of the swaths demonstrate the impact of variable (5%-10%) slab melt addition to each ambient mantle source, which is negligible for Yb, and minor for Nb due to low concentrations of these elements in slab melts (see S4). Fo_{90} primary values were calculated using Petrolog 3.3.1 (Danyushevsky and Plechov, 2011) based on olivine-only models with KD = 0.3, fO_2 = NNO. This results in 10%, 18%, and 20% fractional crystallization corrections for Cerro Negro, Telica, and Masaya lavas, respectively, with primary magmas that correspond to a depleted ambient mantle and extents of melting from 18% (Masaya) to 24% (Cerro Negro). The melt extents determined here are used for calculations of mantle source compositions and forward models in Figs. 5b, 6, and 7. **(b)** Three component binary mixing curves are plotted between ambient mantle, AOC melt, and sediment melts to determine the relative proportion of Sr contributed from each slab component to the arc. The mantle source compositions are calculated from the primary magma compositions and extents of melting determined for the same samples in panel a, based on a non-modal melting model (see S3). The gray field highlights how this diagram constrains the maximum total Sr contribution from the ambient mantle to the arc mantle source to be between 9% and 14%. Black solid lines show the compositional range produced by solid state mixing between the bulk slab components. Open squares are bulk sediment compositions for hemipelagic (blue) and carbonate (orange) sediments. The ambient mantle composition is based on the 'DMM' from Workman and Hart (2005) with $^{87}Sr/^{86}Sr = 0.7028$, which is the composition of unaltered rear-arc basalts from La Providencia Island (Bekaert et al., 2021; Gazel et al., 2011). AOC is assigned $^{87}Sr/^{86}Sr = 0.7032$, with trace element abundances of NMORB from Gale et al. (2013). The AOC melt trace element composition is the 'moderate' T composition from Turner and Langmuir (2022b).

The black solid lines on Fig. 5b show the compositional range produced by solid state mixing between the bulk slab components. This field lies significantly above the arc mantle source compositions. Given that hybrid mélange melting experiments have not produced significant fractionation between Sr and Yb (Codillo et al., 2018), this result conflicts with a model in which slab materials are transferred to the wedge via solid state diapirism (see also, Turner and Langmuir, 2022a). When the slab melts at pressures near the sub-arc slab surface, on the other hand (without being diluted by solid state mixing with wedge peridotites), residual garnet strongly fractionates Sr from Yb. For this reason, we find the slab melting model most consistent with the composition of the arc lavas.

To distinguish between the contributions from hemipelagic vs carbonate sediments, we make use of the ratio Th/Sr, which exhibits a sharp down-core transition from high Th/Sr hemipelagic sediment to low Th/Sr carbonate sediment (Fig. 6e). Fig. 6a shows mixing trajectories between sediment melts and a combined component consisting of 7.5% AOC melt and 92.5% ambient mantle, as established from Fig. 5b (though this ratio has a negligible impact on Th/Sr). Mixing between the combined AOC melt + ambient mantle component and a single bulk subducting sediment composition (70% carbonate, 30% hemipelagic, by mass; black line on Fig. 6a) follows a trajectory that is orthogonal to the arc lava array, confirming that variable recycling efficiencies of the different sediment layers are required. The bulk sediment melt compositions on Fig. 6 are calculated based on the hemipelagic sediment layer with the highest measured Th/Sr, to demonstrate the maximum Th/Sr arc composition that could be produced from any possible bulk sediment mixture. This bulk sediment melt mixing trajectory is unable to reproduce the high Th/Sr of Masaya. To reproduce the Masaya Th/Sr composition, mixing to pure hemipelagic sediment appears to be required (blue field, Fig. 6a). The composition of Cerro Negro can be reproduced by mixing with either bulk sediment or carbonate-dominated sediment compositions (yellow field, Fig. 6a). This suggests that the Masaya mantle source is predominantly overprinted by hemipelagic sediments, whereas Cerro Negro received a greater proportion of subducted marine carbonates.

While differing recycling efficiencies of hemipelagic vs carbonate sediment layers can account for the compositional range of sediment-dominated elements, some other element ratios indicate compositional variability of the AOC melt component. For example, mixing between a single combined AOC melt + ambient mantle component and the full range of sediment melts accounts for a much narrower range of Nd/Sr than observed (Fig. 6b). The high Nd/Sr composition of Masaya could in theory be produced if the total AOC melt addition was lowered, thereby increasing the proportion of Sr derived from the ambient mantle. However, the AOC-ambient mantle mixing ratios are tightly constrained by the Yb/Sr vs $^{87}Sr/^{86}Sr$ diagram (Fig. 5b). As previously discussed, only 9% to 14% of the arc Sr budget can originate from the ambient mantle, and the model shown in Fig. 6b demonstrates the scenario for the maximum allowable (14% Sr) ambient mantle contribution. Instead, the AOC melt composition must vary. This suggests that the relative mobility of light rare earth elements (LREE) in the AOC melt component differs from Masaya to Cerro Negro.

Varying AOC melting temperature provides one possible explanation for the observed Nd/Sr variability. In this framework, AOC melts are not represented by a single fixed composition. Instead, AOC melt compositions vary with slab temperature, as in Turner and Langmuir (2022b), based on an interpolation from compiled piston cylinder experiments (see S4 and Table S3). In these model compositions, hotter AOC melting yields higher Nd/Sr melts due to both greater extents of melting (which dilutes Sr abundances) and the decreased stability of LREE-bearing epidote family minerals (e.g., Klimm et al., 2008; Carter et al., 2015). The full range of Nd/Sr is best reproduced by the variable T slab melt model shown in Figs. 6c-d, where the 'hotter' and 'colder'

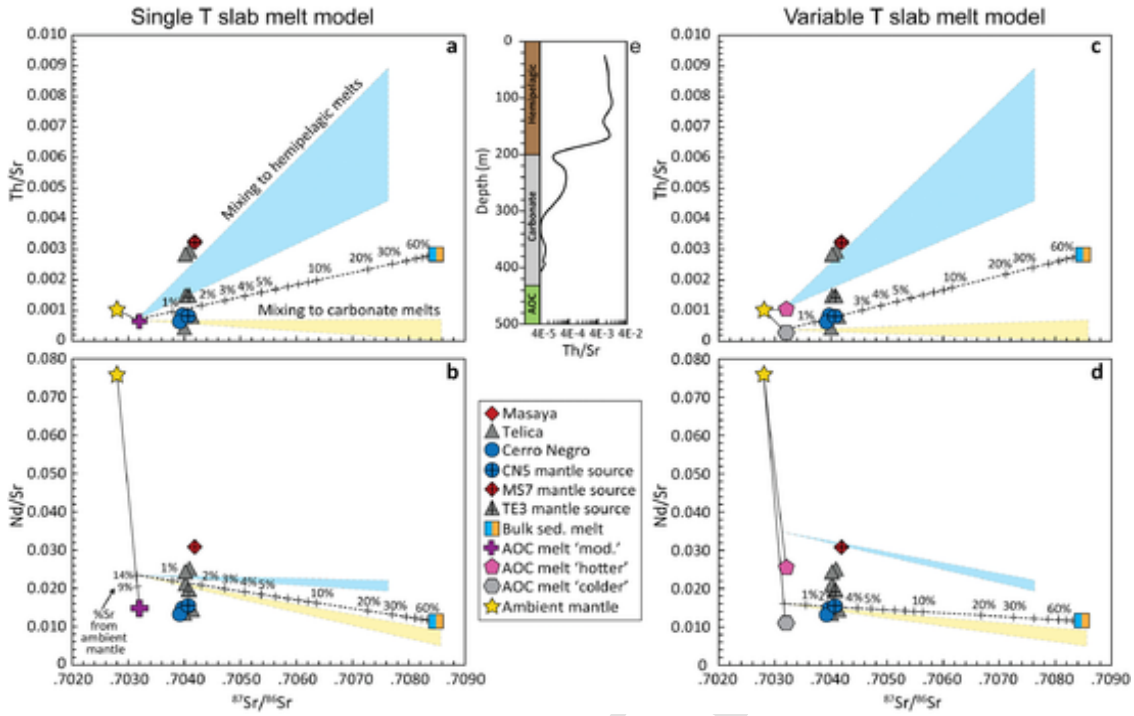

Fig. 6. Th/Sr and Nd/Sr vs $^{87}Sr/^{86}Sr$ mixing lines illustrate the relative contributions of hemipelagic versus carbonate sediments and the effects of variable AOC melt compositions. (a) Th/Sr vs $^{87}Sr/^{86}Sr$ mixing trajectories between an ambient mantle + AOC melt components (as in Fig. 5b), and subducting sediment melt compositions that are based on the range of hemipelagic (blue array) and carbonate (yellow array) sediment compositions from Patino et al. (2000). A mixing line is also shown for an average bulk sediment melt composition based on 70% carbonate to 30% hemipelagic bulk sediment melt (dashed black line). Mantle source compositions for Nicaraguan volcanoes calculated as in Fig. 5b These mixing trajectories show that the high Th/Sr Masaya composition requires a different sediment component than Cerro Negro, consistent with pure hemipelagic sediment. See text and S4 for additional details. **(b)** Nd/Sr vs $^{87}Sr/^{86}Sr$ mixing trajectories based on the same components plotted in panel a show that these components cannot reproduce the full range of lava Nd/Sr values, even given the maximum allowable ambient-mantle Sr contribution (14%). **(c–d)** In these diagrams, the single 'moderate' T AOC melt composition of Turner and Langmuir (2022b) is replaced with the 'colder' and 'hotter' AOC melt compositions, showing that the Masaya composition can be accounted for on both diagrams with hotter AOC melts and nearly pure hemipelagic sediment, whereas Cerro Negro is matched by cooler AOC melts and bulk-sediment compositions. **(e)** Down-core Th/Sr profile of DSDP 495 sediments (from Patino et al., 2000), showing the sharp transition from high-Th/Sr hemipelagic sediment to low-Th/Sr carbonate layers that underpins the contrasting sediment trajectories in **(a)** and **(c)**.

AOC melt compositions replace the single 'moderate' temperature AOC melt used in earlier iterations. The results show that Masaya's composition is consistent with a hotter AOC melt than Cerro Negro with a total of ~7.5% AOC melt addition providing a good fit for both end members. As we note further below, however, slab temperature is not the only parameter that can lead to varied LREE mobility – other important compositional parameters include halogen contents (Li and Hermann, 2017) and oxygen fugacity (as discussed in Turner and Langmuir, 2022b). Importantly, however, even given variable LREE mobility, a nearly pure hemipelagic sediment melt is still required for Masaya and yields the best match for Th/Sr (Fig. 6c), whereas for Cerro Negro the bulk sediment composition remains the closest fit for both Th/Sr and Nd/Sr.

Forward modeling of full trace element patterns can be used to further evaluate whether the variations in mantle melting, sediment proportions, and slab temperatures established above can adequately account for the differing trace element compositions of Cerro Negro and Masaya. The goal of this modeling approach is to determine whether the hypothesized melting conditions and mixing proportions of slab and mantle components produce a reasonable approximation to the full incompatible trace element patterns. Extents of melting and ambient mantle compositions follow Fig. 5a (F = 18% and 24% for Cerro Negro and Masaya models, respectively). Both models incorporate 2.3% sediment melt and 7.5% AOC melt, calculated as in Turner and Langmuir (2022b). Separate models were run for each hemipelagic sediment layer composition, with the full range of resulting compositions shown as gray fields in Fig. 7. The Masaya model is based on hemipelagic sediment only (no carbonate) and 'hotter' AOC melt, whereas the Cerro Negro model is based on a bulk sediment composition and 'colder' AOC melt. Additional details of the model can be found in S3 and S4.

As shown on Fig. 7, the trace element model generally produces a good match to the data and accounts well for the most salient compositional differences between the two geochemical end members, including the slopes of REE abundances and fractionations between REE, Sr, HFSE, and LILE. Most model runs overestimate arc Ba abundances, consistent with Ba loss at shallow forearc depths (Peccia et al., 2025; Solomon and Kastner, 2012). The model also slightly overestimates Zr and Hf. This may be because the AOC melt compositions are based on NMORB (Gale et al., 2013), whereas the subducting mafic crust offshore Nicaragua is variably enriched (Herbrich et al., 2015). If the subducting mafic crust was initially more enriched, AOC melts would have higher Sr abundances, whereas Zr concentrations would remain buffered by residual zircon. With a more enriched ocean crust, a successful model would require somewhat lower AOC melt additions to the mantle source, though this would not significantly impact the interpretations presented above.

In summary, these observations demonstrate the value of utilizing full trace element forward modeling for arcs and confirm that the observed trace element variability between these geochemical end members can be plausibly reproduced with three parameters: extent of mantle melting, sediment recycling efficiency, and slab temperature. In Section 5.3 we discuss potential mechanisms that could produce varia-

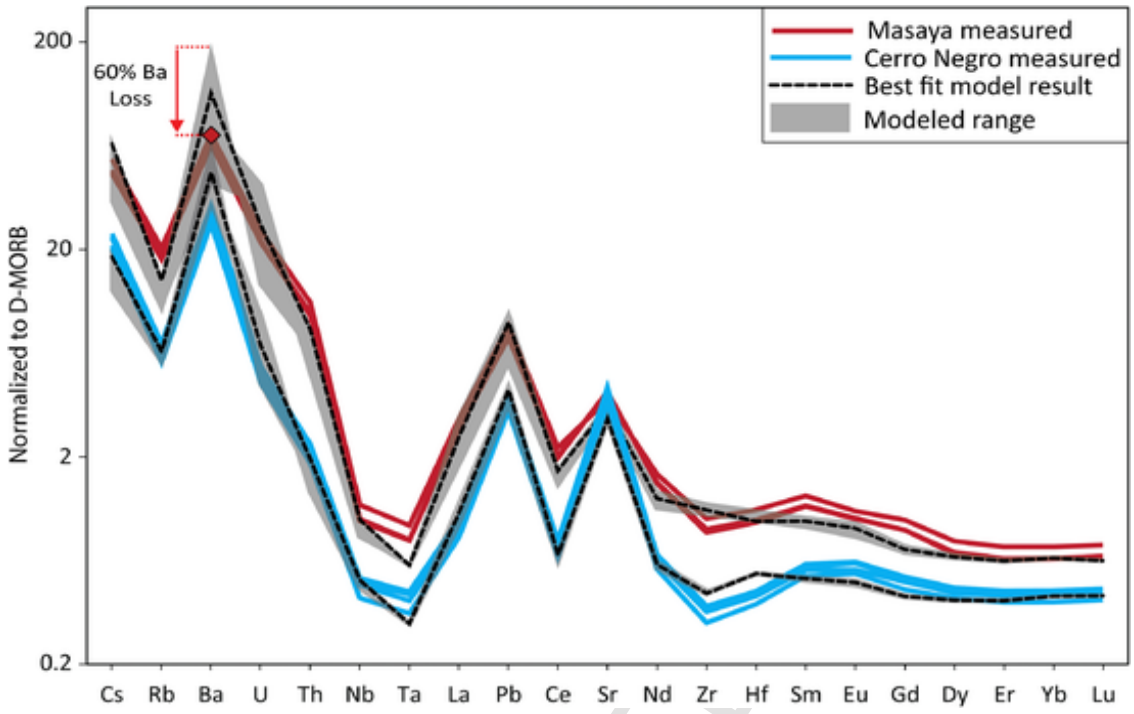

Fig. 7. Forward models of incompatible trace element patterns match compositions of Cerro Negro and Masaya volcanoes. Shaded regions are the range of modeled trace element compositions for Masaya and Cerro Negro volcanoes, accounting for variability in hemipelagic sediment compositions. Black dashed lines are best-fit model results. Solid red and blue lines are measured literature values for Masaya and Cerro Negro, respectively. The red diamond shows how a 60% loss of Ba from the sediments in the forearc can account for the Ba mismatch in the trace element abundance models and reflects the model results with the highest Ba concentrations. Measured values include only ''Quality 35' data from Carr et al., (2014). Normalized to DMORB (Gale et al., 2013). Modeling parameters are based on ambient mantle compositions and extents of melting constrained via Fig. 5a and slab component proportions based on Figs. 6c-d. Detailed compositions of slab components and melting calculations can be found in S3, S4, and Table S3.

tions in slab T as well as alternative hypotheses to explain the increased LREE mobility required for Masaya.

5.2. *Evaluating $\delta^{88}Sr$ as an additional tracer of subduction recycling*

The distinct $\delta^{88}Sr$ compositions of marine carbonates (Fig. 3) underpinned the motivation to develop this system as a proxy of carbon recycling. At present, interpretation of arc $\delta^{88}Sr$ data suffers from limited high-precision MORB and AOC data, which are needed to fully evaluate the range of $\delta^{88}Sr$ in the upper mantle and the effects of ocean crust alteration. When assessed within the framework provided by trace element and radiogenic isotope data, however, we find that this geochemical tool may already have broad utility as a tracer of subduction processes.

Key results from the prior section include: 1) The differing trace element patterns of Cerro Negro and Masaya, exemplified by Th/Sr (Fig. 6a,c) are most consistent with a sediment melt contribution similar to the bulk subducted sediment composition for Cerro Negro, but dominated by the hemipelagic sediment for Masaya. 2) The overall enrichment in sediment-derived trace element abundances is reproduced by 2.3% sediment melt added to the mantle source for both Cerro Negro and Masaya (Fig. 7). 3) Given sediment melts with $^{87}Sr/^{86}Sr$~0.708 and arc lavas with $^{87}Sr/^{86}Sr$~0.704, the combined composition of the remaining (ambient mantle + AOC melt) components must be $^{87}Sr/^{86}Sr$~0.7032. 4) Variation in Nd/Sr is not consistent with differing sediment proportions but can be accounted for by differing AOC melt compositions.

On a diagram of $^{87}Sr/^{86}Sr$ vs $\delta^{88}Sr$ (Fig. 8a), where mixing is linear, the composition of Cerro Negro should lie on a line between the bulk sediment and the combined composition of AOC melt and ambient mantle components that comprise its mantle source. The combined AOC melt + ambient mantle component must therefore have $\delta^{88}Sr$ ~0.345‰ (black triangle, Fig. 8a). Carrying out the same exercise for Masaya, based on the hemipelagic sediment composition, results in a combined AOC melt + ambient mantle composition of $\delta^{88}Sr$ ~0.245‰ (white triangle, Fig. 8a).

Though differing sediment proportions can strongly control certain trace element abundances and ratios (e.g. Fig. 2, Figs. 6–7), the similar $\delta^{88}Sr$ of the sediments and the dominant influence of AOC-derived Sr (e.g., Fig. 5b) strictly limit the extent to which subducting sediments influence mantle source $\delta^{88}Sr$. This is illustrated on Fig. 8a by the blue field, which extends from the Cerro Negro ambient mantle + AOC melt composition (black triangle) to the individual sediment end members. This field shows that within the relatively narrow range of the arc lava $^{87}Sr/^{86}Sr$ compositions, varied sediment compositions can produce a maximum of ~0.02‰ variation in $\delta^{88}Sr$ (based on the highest $\delta^{88}Sr$ carbonate sample). The same is true for a mixing field for Masaya (gray field).

The ambient mantle composition also has a negligible influence on $\delta^{88}Sr$, because the proportion of Sr in the arc lavas that originates from the ambient mantle is small. The Sr/Yb vs $^{87}Sr/^{86}Sr$ diagram (Fig. 5b) shows that only 9% to14 % of the Sr in the combined AOC melt + ambient mantle component can originate from the mantle. Given this constraint, the red field in Fig. 8b depicts the range of possible compositions that can be produced by mixing between subducting sediments, an AOC melt component with $\delta^{88}Sr$~0.36‰ (required to produce a field that overlaps Cerro Negro), and an ambient mantle component with $\delta^{88}Sr$~0.34‰, which is the highest measured $\delta^{88}Sr$ MORB value (via MC-ICP-MS, Amsellem et al., 2018). The brown field then shows how the mixing domain would change if sediment and AOC compositions re-

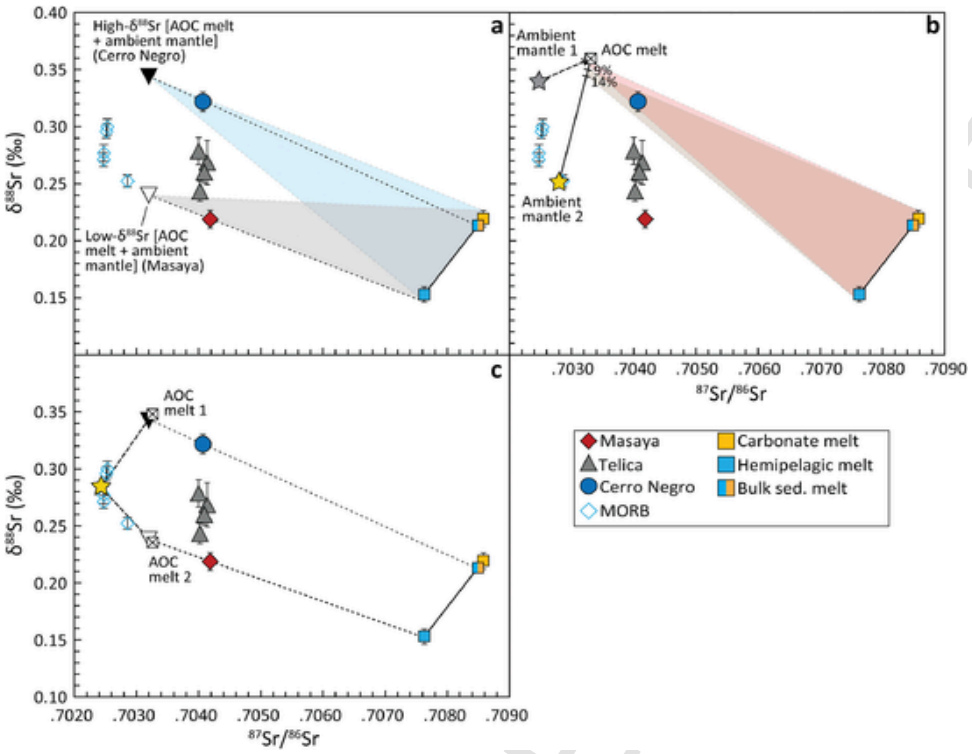

Fig. 8. $^{87}Sr/^{86}Sr$ vs $\delta^{88}Sr$ diagrams showing mixing scenarios to account for end-member compositions represented by Masaya and Cerro Negro. (a) A high $\delta^{88}Sr$ AOC + ambient mantle slab component can account for the high $\delta^{88}Sr$ Cerro Negro lava end member while an additional low $\delta^{88}Sr$ AOC + ambient mantle slab component is needed to explain Masaya. No single high or low $\delta^{88}Sr$ AOC + ambient mantle component mixing with any combination of sediment can reproduce the full range of arc lava $\delta^{88}Sr$. **(b)** $\delta^{88}Sr$ further highlights how AOC is the primary control on Sr. Adding more Sr to the slab from an ambient mantle source within the allowable range of 9% to 14% (based on Fig. 5b) has a negligible effect on $\delta^{88}Sr$. The red and brown mixing arrays also demonstrate how mantle source variability cannot account for differences in the slab $\delta^{88}Sr$. **(c)** Schematic model showing how a single ambient mantle source with MORB-like $\delta^{88}Sr$ (~0.28‰), varied AOC melt $\delta^{88}Sr$, and sediment $\delta^{88}Sr$ can reproduce Masaya and Cerro Negro end members and explain the range of arc lava $\delta^{88}Sr$ compositions. Tie lines between sediments are only plotted for the higher $\delta^{88}Sr$ carbonate sample (495-37R4-20-21) as the goal of these models is to assess the maximum possible $\delta^{88}Sr$ variability that can be inherited from the sediments to the arc.

mained the same, but the ambient mantle composition shifted down to $\delta^{88}Sr$~0.25‰, which is the lowest measured $\delta^{88}Sr$ MORB value. The two fields are barely offset from one another, confirming that varying ambient mantle composition cannot account for the $\delta^{88}Sr$ range of the arc.

The most likely explanation for the $\delta^{88}Sr$ variability of the Nicaraguan arc lavas is therefore compositional variability of AOC melts, which provide the predominant source of Sr to the arc and apparently span a greater compositional range than existing $\delta^{88}Sr$ TIMS measurements of MORB. A schematic model with a single ambient mantle $\delta^{88}Sr$, varied AOC melt $\delta^{88}Sr$, and sediment proportions determined from Figs. 5–6 is shown on Fig. 8c.

The AOC melt $\delta^{88}Sr$ composition added to the Cerro Negro mantle is constrained to be >0.34‰, which is higher than the range measured in the ODP site 801C composite AOC samples (Fig. 4). Higher $\delta^{88}Sr$ is also apparent for Oshima (JB-2), and two Marianas samples. The original mantle source of the site 801C basalts must have had particularly low $\delta^{88}Sr$ (given $\delta^{88}Sr$~0.25‰ in the least altered composite samples), however, and Sr exchange during alteration at this site appears to have been inhibited (relative to other cores) by off-axis volcanism. It is thus likely that the 801C samples do not adequately represent the compositional range of subducted mafic ocean crust in our study region (see S5 for an extended discussion of this issue).

In summary, the $\delta^{88}Sr$ systematics support varying AOC melt compositions, which are presumably inherited from $\delta^{88}Sr$ heterogeneity of the subducting mafic crust (absent some unrecognized fractionation during slab melting). Differing AOC melt compositions are also consistent with the observed variability of Nd/Sr. Together, the trace element and isotopic diversity of Nicaraguan arc lavas appears to require covariation in the slab-to-arc recycling efficiency of different sediment layers alongside variability in AOC melt composition.

5.3. A geochemical signal from subducting seamounts?

The subducting seamounts on the Cocos plate provide a plausible explanation for the varied recycling efficiencies of the two sediment layers alongside a variable $\delta^{88}Sr$ composition of AOC melts. In the Central American segment of the Cocos plate, intra-plate seamounts emplaced at ~11 Ma (Fig. 1a) coincide with the regional 'carbonate crash,' when carbonate sediment deposition ceased (Plank et al., 2002; Herbrich et al., 2015). Seamounts emplaced after the carbonate crash would cover the older carbonate layers and eventually be blanketed by younger hemipelagic sediment, placing hundreds of meters of basalt between the two sediment units. During subduction, portions of the slab without seamounts would consist of typical AOC overlain by carbonate and hemipelagic sediment, producing slab melts with both sediment components and 'typical' Cocos plate AOC signatures, as inferred for Cerro Negro (Fig. 9a). In contrast, where an <11 Ma seamount enters the trench, slab melts would primarily sample seamount-derived crust plus overlying hemipelagic sediment while the underlying carbonate layer would be shielded from the slab–mantle interface, yielding the hemipelagic-dominated sediment signature observed for Masaya (Fig. 9b).

Seamount emplacement may also introduce compositional heterogeneity into the subducting mafic ocean crust. Cocos plate seamount

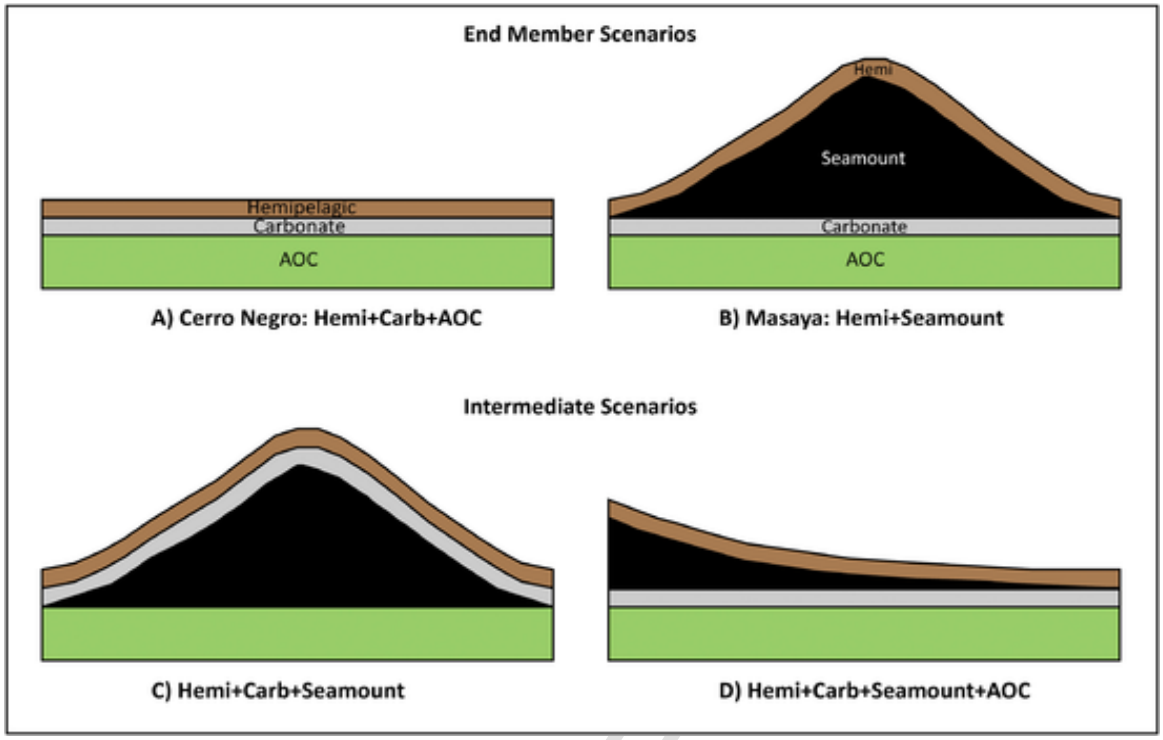

Fig. 9. Conceptual models showing simplified slab surface of down-going Cocos plate for several Nicaraguan subduction scenarios. (a) reflects normal subduction in which a mixture of AOC and hemipelagic + carbonate sediments are added from the slab to the arc. In **(b)**, large seamounts on the Cocos plate erupted after the carbonate crash effectively cover the carbonate sediments and underlying AOC. **(c)** and **(d)** represent intermediate scenarios in which various proportions of each component could reach the arc.

lavas display a wide range of $^{87}Sr/^{86}Sr$ values (0.7025–0.7031), reflecting mantle components from both the Galápagos plume and Eastern Pacific Rise (Herbrich et al., 2015). Given this wide range in $^{87}Sr/^{86}Sr$, the seamounts may also have variable $\delta^{88}Sr$, ranging to lower $\delta^{88}Sr$, as observed in some OIBs (Fig. 3), and potentially accounting for the low $\delta^{88}Sr$ composition of Masaya. Though strontium exchange during hydrothermal alteration should shift ocean crust $\delta^{88}Sr$ compositions closer to seawater, subducting seamounts are likely to become 'decapitated', with only the lowermost sections of the seamounts being subducted beneath the volcanic arc (Cloos and Shreve, 1996; McIntosh et al., 2007; Watts et al., 2010). Because seawater–rock Sr exchange is largely confined to the uppermost basaltic layers (Révillon et al., 2007; Teagle et al., 1999), decapitation of seamounts in the subduction channel may leave behind a layer of oceanic crust that is more representative of the seamount's mantle source. As such, the high $\delta^{88}Sr$ composition of Cerro Negro may be inherited from normal MORB-like oceanic crust modified by hydrothermal alteration, whereas the low $\delta^{88}Sr$ composition of Masaya may be inherited from a subducting seamount following decapitation. This hypothesis thus provides a consistent mechanism to account for the covariation of the recycling efficiencies of the two sediment layers and the $\delta^{88}Sr$ composition of the AOC melt component.

Seamount subduction also has the potential to enhance the subducting flux of younger (high $^{10}Be/^{9}Be$) sediments by plowing down material from the toe of the accretionary prism (Bangs et al., 2006; Dominguez et al., 1998; von Huene et al., 2000), which in our study region are compositionally similar to the Cocos plate hemipelagic sediment (Kimura et al., 1997). Following decapitation, some fraction of the sediments piled up along the leading edge of the seamount would likely be drawn into the subduction channel, providing a mechanism for the enhanced flux of hemipelagic material to Masaya while inhibiting the transfer of the deeper carbonate layers, which remain trapped beneath a thick layer of basalt.

A remaining question is whether a seamount subduction scenario also directly accounts for variability of AOC melt Nd/Sr (Fig. 6). While it is well documented that seamounts can affect temperature distributions within a down-going plate, these effects are complex (e.g., Spinelli and Harris, 2011). To test this hypothesis, we ran conductive cooling and hydrothermal circulation models of a 15 km wide, 1.5 km tall seamount emplaced on 10 Ma ocean crust. The model results show that the initial heat added by seamount emplacement will have dissipated within 1 Ma, long before subduction begins (Fig. S3a). However, subsequent hydrothermal circulation can generate significant thermal gradients across the edifice, with positive temperature anomalies (>60°C) multiple km wide across the seamount core that persist far longer (10–20 Ma, Fig. S3b). If a seamount with this thermal profile were to later be decapitated, it may produce a transient positive slab surface temperature anomaly. In other cases, hydrothermal outfluxes from a seamount appear to be fed by recharge from more distal sites, resulting in a uniformly elevated temperature profile across the seamount edifice that would further enhance this effect (Fisher et al., 2003a; Fisher et al., 2003b). Fisher et al. (2003b) present evidence that the Cocos plate thermal structure has been impacted by widespread hydrothermal circulation through seamounts. While the net effect on heat flow is negative, in detail these seamounts should impart significant heterogeneity on the temperature gradient, with either negative or positive anomalies associated with individual seamounts (see S6 for an extended discussion). Together, these considerations support the possibility that the slab surface beneath Masaya consists of seamount-modified crust that is both compositionally distinct and hotter than neighboring segments, producing AOC-derived melts with higher LREE abundances and Nd/Sr than those beneath Cerro Negro, despite similar sub-arc slab depths.

Seamounts are not the only process capable of producing localized slab-temperature differences, however, and similar thermal anomalies could arise even in their absence. Seismic studies have identified along-

strike variability in mantle wedge attenuation and wave speeds for different Central American Arc segments, indicating potential thermal heterogeneities (e.g., Rychert et al., 2008). Differences in slab temperatures beneath Masaya and Cerro Negro may thus reflect broader along-arc segmentation. Additionally, although geochemical indices commonly interpreted as slab-temperature proxies largely track LREE mobility during slab melting, several other mechanisms can produce comparable effects (e.g., Skora and Blundy, 2012). For example, less oxidized lithologies should reduce the stability of epidote-group minerals that host LREEs (as discussed in Turner and Langmuir, 2022b), enhancing LREE mobility independently of temperature changes. It is plausible that seamount decapitation would strip away the oxidized, seawater-altered upper basaltic layers most capable of stabilizing epidote, leaving deeper, more reduced crustal sections (Alt et al., 1986) that release a larger fraction of their initial LREE budgets upon melting.

Taken together, these observations suggest that the subduction of seamounts which postdate the carbonate crash in Central America provides a consistent framework for understanding the along-arc geochemical variability in Nicaragua. By modifying sediment stratigraphy, introducing compositionally distinct and variably altered mafic crust, and generating thermal and/or redox heterogeneities in the subducting slab, seamounts offer a mechanism that can simultaneously explain Masaya's low δ^{88}Sr, reduced carbonate input, and elevated LREE mobility. Intermediate scenarios involving older seamounts, partially decapitated edifices, or thin volcaniclastic caps could yield mixtures of both sediments, AOC, and seamount material within the upper slab, producing the transitional trace element compositions and δ^{88}Sr observed among Telica lavas (Fig. 9c-d). While alternative processes, such as slab segmentation or variations in oxidation state, may also contribute, the spatial coincidence of seamount-modified crust and the specific geochemical requirements of Masaya indicate that subducting seamounts provide a plausible and unifying mechanism for the observed variations.

5.4. Implications for magmatic CO_2 flux and carbon recycling in Central America

The Nicaraguan Sr isotope and trace element systematics provide constraints on the arc's Sr budget that can be used to independently estimate the carbonate recycling efficiency from the slab to the arc. In our best fit model of Cerro Negro, 57 ppm Sr (out of a total of 300 ppm Sr) originates from marine carbonate. The Nicaraguan Arc segment is estimated to erupt ~3.9×10^7 kg/yr of lava and tephra per km arc (Freundt et al., 2014). Assuming an intrusive:extrusive ratio ranging from 5 to 7 (a reasonable range for thin and relatively mafic arc crust; White et al., 2006), this translates to a magmatic flux of ~11,000 to 15,600 kg/yr/km of carbonate-derived Sr. The Cocos plate carries 200 m of marine carbonate with ~1500 ppm Sr into the trench at 71 km/Ma (Syracuse et al., 2010), which translates to ~37,000 kg/yr/km of subducting carbonate-derived Sr. The recycling efficiency of carbonate-derived Sr from the slab to the arc is thus approximately 30%-42%.

Extrapolation from Sr recycling efficiency to bulk carbonate recycling efficiency depends importantly on the assumed mechanism of carbon transfer from the slab to the arc. As discussed in detail by Schettino and Poli (2020), most modern experimental studies have focused on phase relationships of carbonated pelites similar in composition to the GLOSS sediment average of Plank (2014). These experimental results are not directly relevant to the systematics of subducting Coco's plate sediments, however, which include 200 m of nearly pure carbonate. Experiments of hydrous carbonate-dominated systems show that voluminous hydrous carbonatitic melts will be generated at temperatures as low as 650˚C (Durand et al., 2015; Foustoukos and Mysen, 2014; Schettino and Poli, 2020; Wyllie and Boettcher, 1969). A model of hydrous slab melting for both carbonate and other materials along the slab surface is thus favored.

If subducted marine carbonate is largely transferred to the Nicaraguan Arc mantle source by hydrous carbonatitic melts, then the minimum carbonate recycling efficiency can be reasonably estimated as the extent of carbonate melting. If $DSr^{solid/melt} \sim 2$ (Carter et al., 2015) for bulk carbonate sediment melting, then 45% to 60% of Sr will be extracted from the melting carbonate with a melt fraction of ~0.45 to ~0.6. While future work is undoubtedly needed to better constrain the parameters used in this calculation, the constraints from Sr isotope and trace element data currently indicate that approximately 50% of subducted carbonate may be transported to the arc mantle source by a hydrous carbonatitic melt. Subducting seamounts may have the ability to cover the carbonate layer and transiently reduce carbonate recycling efficiency. While this result is preliminary, we note that it is broadly consistent with estimates based on direct measurements of gas abundance and isotope ratios (e.g. de Moor et al., 2017; Barry et al., 2019).

6. Conclusions

This study reveals large δ^{88}Sr variations within an arc, extending both lower and higher than published values for MORB and AOC. Because the arc Sr budget is overwhelmingly controlled by AOC-derived melt contributions, the observed isotopic variability likely originates from the mafic ocean crust rather than the ambient mantle or sediments. Differing lava trace element patterns are most consistent with a sediment melt contribution to Cerro Negro that resembles the bulk subducted sediment composition, whereas the sediment contribution to Masaya is mostly hemipelagic, as previously demonstrated by Patino et al., 2000. Masaya lavas also exhibit elevated Nd/Sr, which cannot be attributed to differences in the total contribution of AOC melt, and instead provide additional support for variable AOC melt compositions controlled by slab temperature. The combined trace element, radiogenic, and stable isotope systematics therefore suggest that the relative input of carbonate vs hemipelagic sediment to the arc covaries with the composition and temperature of the subducting mafic crust.

By changing sediment stratigraphy, introducing isotopically distinct and variably altered basaltic crust, and generating localized thermal heterogeneities within the subducting slab, the subduction of seamounts emplaced on the Cocos plate following the 11 Ma carbonate crash offers a coherent mechanism capable of reproducing the observed geochemical systematics in Nicaragua. This process can simultaneously account for Masaya's low δ^{88}Sr, diminished carbonate contribution, and elevated LREE mobility, while Cerro Negro's high δ^{88}Sr instead derives from a typical MORB-like AOC. While future measurements of seamount δ^{88}Sr are required to confirm our model, given the documented isotopic diversity of the Galapagos hotspot-influenced seamounts (Herbrich et al., 2015) and large variability of OIB δ^{88}Sr, they likely also possess variable δ^{88}Sr, including lighter values consistent with Masaya. This testable hypothesis integrates trace element, radiogenic Sr, and stable Sr isotope constraints, with implications for other arc systems as suggested by global comparisons (see S7 for an extended discussion).

Lastly, we estimate that at least ~45% to 60% of carbon from subducted carbonate sediment is recycled back to the surface via arc magmatism—consistent with gas-flux constraints but independently derived here using trace elements and Sr isotopes. Overall, this work demonstrates the power of Sr stable isotopes in arc settings, offering new insights into slab recycling processes, the origins of geochemical diversity in Central American arc magmas, and the long-term co-evolution of Earth's mantle and surface reservoirs.

Funding sources

This work was supported by the National Science Foundation (Grant No. 1939080).

Data availability

All data used in this study are available in main text or supplementary materials.

Uncited references

CRediT authorship contribution statement

Alexander J. Hammerstrom: Writing – review & editing, Writing – original draft, Visualization, Validation, Software, Project administration, Methodology, Investigation, Formal analysis, Data curation. **Rita Parai:** Writing – review & editing, Validation, Resources, Methodology, Funding acquisition, Formal analysis, Conceptualization. **Richard W. Carlson:** Writing – review & editing, Validation, Supervision, Resources, Project administration, Formal analysis. **Vlad C. Manea:** Writing – review & editing, Visualization, Software, Resources, Investigation, Formal analysis. **Marina Manea:** Writing – review & editing, Visualization, Software, Resources, Investigation, Formal analysis. **Stephen J. Turner:** Writing – review & editing, Validation, Supervision, Software, Project administration, Methodology, Investigation, Funding acquisition, Formal analysis, Data curation, Conceptualization.

Declaration of competing interest

The authors declare that they have no known competing financial interests or personal relationships that could have appeared to influence the work reported in this paper.

Acknowledgments

We thank Isaac Larson for use of clean lab facilities, Stephen Eyles for providing space and technical assistance with quadrupole ICP-MS analyses, and Timothy Mock for this technical assistance with TIMS analyses. We thank Mike Carr and Esteban Gazel for providing the Nicaraguan lava samples and Terry Plank for providing the 801C composite samples. DSDP 495 sediment samples were provided by the International Ocean Discovery Program (IODP) Gulf Coast Repository. This work was supported by NSF grant EAR-1939080.

Data availability

Data will be made available on request.

Supplementary materials

Supplementary material associated with this article can be found, in the online version, at doi:10.1016/j.epsl.2026.119829.

References

Alt, J.C., Honnorez, J., Laverne, C., Emmermann, R., 1986. Hydrothermal Alteration of a 1-Km Section through the Upper Oceanic-Crust, Deep-Sea Drilling Project Hole 504b - Mineralogy, Chemistry, and Evolution of Seawater-Basalt Interactions. J Geophys Res-Solid 91, 309–335. https://doi.org/10.1029/JB091iB10p10309.

Amsellem, E., Moynier, F., Day, J.M.D., Moreira, M., Puchtel, I.S., Teng, F.Z., 2018. The stable strontium isotopic composition of ocean island basalts, mid-ocean ridge basalts, and komatiites. Chem. Geol. 483, 595–602. https://doi.org/10.1016/j.chemgeo.2018.03.030.

Aubouin, J., Von Huene, R., 1982. Site 495; Cocos plate, Middle America trench outer slope. Init. Rep. DSDP 67, 79–141.

Averyt, K.B., Paytan, A., Li, G., 2003. A precise, high-throughput method for determining Sr/Ca, Sr/Ba, and Ca/Ba ratios in marine barite. Geochem., Geophys., Geosyst. 4. https://doi.org/10.1029/2002gc000467.

Bangs, N.L.B., Gulick, S.P.S., Shipley, T.H., 2006. Seamount subduction erosion in the Nankai Trough and its potential impact on the seismogenic zone. Geology. 34. https://doi.org/10.1130/g22451.1.

Barry, P.H., de Moor, J.M., Giovannelli, D., Schrenk, M., Hummer, D.R., Lopez, T., Pratt, C.A., Segura, Y.A., Battaglia, A., Beaudry, P., Bini, G., Cascante, M., d'Errico, G., di Carlo, M., Fattorini, D., Fullerton, K., Gazel, E., Gonzalez, G., Halldorsson, S.A., Iacovino, K., Ilanko, T., Kulongoski, J.T., Manini, E., Martinez, M., Miller, H., Nakagawa, M., Ono, S., Patwardhan, S., Ramirez, C.J., Regoli, F., Smedile, F., Turner, S., Vetriani, C., Yucel, M., Ballentine, C.J., Fischer, T.P., Hilton, D.R., Lloyd, K.G., 2019. Forearc carbon sink reduces long-term volatile recycling into the mantle. Nature 568, 487–492. https://doi.org/10.1038/s41586-019-1131-5.

Bekaert, D.V., Gazel, E., Turner, S., Behn, M.D., de Moor, J.M., Zahirovic, S., Manea, V.C., Hoernle, K., Fischer, T.P., Hammerstrom, A., Seltzer, A.M., Kulongoski, J.T., Patel, B.S., Schrenk, M.O., Halldorsson, S.A., Nakagawa, M., Ramirez, C.J., Krantz, J.A., Yucel, M., Ballentine, C.J., Giovannelli, D., Lloyd, K.G., Barry, P.H., 2021. High (3) He/(4)He in central Panama reveals a distal connection to the Galapagos plume. Proc. Natl. Acad. Sci. u S. a 118. https://doi.org/10.1073/pnas.2110997118.

Bolge, L.L., Carr, M.J., Milidakis, K.I., Lindsay, F.N., Feigenson, M.D., 2009. Correlating geochemistry, tectonics, and volcanic volume along the Central American volcanic front. Geochem., Geophys., Geosyst. 10. https://doi.org/10.1029/2009gc002704.

Carr, M.J., Feigenson, M.D., Bolge, L.L., Walker, J.A., Gazel, E., 2014. RU_CAGeochem, a database and sample repository for Central American volcanic rocks at Rutgers University. Geosci. Data J. 1, 43–48. https://doi.org/10.1002/gdj3.10.

Carter, L.B., Skora, S., Blundy, J.D., De Hoog, J.C.M., Elliott, T., 2015. An experimental study of trace element fluxes from subducted oceanic crust. J. Petrol. 56, 1585–1606. https://doi.org/10.1093/petrology/egv046.

Cloos, M., Shreve, R.L., 1996. Shear-zone thickness and the seismicity of Chilean- and Marianas-type subduction zones. Geology. 24. https://doi.org/10.1130/0091-7613(1996)024<0107:Sztats>2.3.Co;2.

McIntosh, K.D., Silver, E.A., Ahmed, I., Berhorst, A., Ranero, C.R., Kelly, R.K., Flueh, E.R., 2007. In: Dixon, T.H., Moore, C. (Eds.), The Seismogenic Zone of Subduction Thrust Faults 9. The Nicaragua Convergent Margin: Seismic Reflection Imaging of the Source of a Tsunami Earthquake. Columbia University Press, pp. 257–287. https://doi.org/10.7312/dixo13866.

Codillo, E.A., Le Roux, V., Marschall, H.R., 2018. Arc-like magmas generated by melange-peridotite interaction in the mantle wedge. Nat. Commun. 9, 2864. https://doi.org/10.1038/s41467-018-05313-2.

Danyushevsky, L.V., Plechov, P., 2011. Petrolog3: Integrated software for modeling crystallization processes. Geochem., Geophys., Geosyst. 12. https://doi.org/10.1029/2011gc003516.

Dasgupta, R., Hirschmann, M.M., 2010. The deep carbon cycle and melting in Earth's interior. Earth. Planet. Sci. Lett. 298, 1–13. https://doi.org/10.1016/j.epsl.2010.06.039.

de Moor, J.M., Kern, C., Avard, G., Muller, C., Aiuppa, A., Saballos, A., Ibarra, M., LaFemina, P., Protti, M., Fischer, T.P., 2017. A new sulfur and carbon degassing inventory for the southern central American volcanic arc: the importance of accurate time-series data sets and possible tectonic processes responsible for temporal variations in arc-scale volatile emissions. Geochem., Geophys., Geosyst. 18, 4437–4468. https://doi.org/10.1002/2017gc007141.

Dominguez, S., Lallemand, S.E., Malavieille, J., von Huene, R., 1998. Upper plate deformation associated with seamount subduction. Tectonophysics. 293, 207–224. https://doi.org/10.1016/s0040-1951(98)00086-9.

Durand, C., Baumgartner, L.P., Marquer, D., 2015. Low melting temperature for calcite at 1000 bars on the join CaCO3-H2O – some geological implications. Terra Nova 27, 364–369. https://doi.org/10.1111/ter.12168.

Dymond, J., Suess, E., Lyle, M., 1992. Barium in deep-sea sediment: a geochemical proxy for paleoproductivity. Paleoceanography 7, 163–181. https://doi.org/10.1029/92pa00181.

Elliott, T., 2004. Tracers of the slab, inside the subduction factory, J. Eiler (Ed.), 23–45. 10.1029/138GM03

Fisher, A.T., Davis, E.E., Hutnak, M., Spiess, V., Zuhlsdorff, L., Cherkaoui, A., Christiansen, L., Edwards, K., Macdonald, R., Villinger, H., Mottl, M.J., Wheat, C.G., Becker, K., 2003a. Hydrothermal recharge and discharge across 50 km guided by seamounts on a young ridge flank. Nature 421, 618–621. https://doi.org/10.1038/nature01352.

Fisher, A.T., Stein, C.A., Harris, R.N., Wang, K., Silver, E.A., Pfender, M., Hutnak, M., Cherkaoui, A., Bodzin, R., Villinger, H., 2003b. Abrupt thermal transition reveals hydrothermal boundary and role of seamounts within the Cocos Plate. Geophys. Res. Lett. 30. https://doi.org/10.1029/2002gl016766.

Foustoukos, D.I., Mysen, B.O., 2014. The structure of water-saturated carbonate melts. Am. Mineral. 100, 35–46. https://doi.org/10.2138/am-2015-4856.

Freundt, A., Grevemeyer, I., Rabbel, W., Hansteen, T.H., Hensen, C., Wehrmann, H., Kutterolf, S., Halama, R., Frische, M., 2014. Volatile (H2O, CO2, Cl, S) budget of the Central American subduction zone. Int. J. Earth Sci. 103, 2101–2127. https://doi.org/10.1007/s00531-014-1001-1.

Gale, A., Dalton, C.A., Langmuir, C.H., Su, Y., Schilling, J.G., 2013. The mean composition of ocean ridge basalts. Geochem., Geophys., Geosyst. 14, 489–518. https://doi.org/10.1029/2012gc004334.

Gazel, E., Hoernle, K., Carr, M.J., Herzberg, C., Saginor, I., den Bogaard, P.v., Hauff, F., Feigenson, M., Swisher, C., 2011. Plume–subduction interaction in southern Central America: Mantle upwelling and slab melting. Lithos 121, 117–134. https://doi.org/10.1016/j.lithos.2010.10.008.

Hayes, G.P., Moore, G.L., Portner, D.E., Hearne, M., Flamme, H., Furtney, M., Smoczyk,

G.M., 2018. Slab2, a comprehensive subduction zone geometry model. Science (1979) 362, 58–61. https://doi.org/10.1126/science.aat4723.
Herbrich, A., Hoernle, K., Werner, R., Hauff, F., Bogaard, P.v.d., Garbe-Schönberg, D., 2015. Cocos plate Seamounts offshore NW Costa Rica and SW Nicaragua: Implications for large-scale distribution of Galápagos plume material in the upper mantle. Lithos. 212–215, 214–230. https://doi.org/10.1016/j.lithos.2014.10.014.
Hermann, J., Spandler, C.J., 2008. Sediment melts at sub-arc depths: an experimental study. J. Petrol. 49, 717–740. https://doi.org/10.1093/petrology/egm073.
Heydolph, K., Hoernle, K., Hauff, F., Bogaard, P.v.d., Portnyagin, M., Bindeman, I., Garbe-Schönberg, D., 2012. Along and across arc geochemical variations in NW Central America: Evidence for involvement of lithospheric pyroxenite. Geochim. Cosmochim. Acta 84, 459–491. https://doi.org/10.1016/j.gca.2012.01.035.
Kelemen, P.B., Manning, C.E., 2015. Reevaluating carbon fluxes in subduction zones, what goes down, mostly comes up. Proc. Natl. Acad. Sci. u S. a 112, E3997–E4006. https://doi.org/10.1073/pnas.1507889112.
Kelley, K.A., Plank, T., Ludden, J., Staudigel, H., 2003. Composition of altered oceanic crust at ODP Sites 801 and 1149. Geochem., Geophys., Geosyst. 4. https://doi.org/10.1029/2002gc000435.
Kimura, G., Silver, E.A., Blum, P., et al., 1997. Proc. ODP, Init. Repts., 170. Ocean Drilling Program, College Station, TX. https://doi.org/10.2973/odp.proc.ir.170.1997.
Klaver, M., Davies, G.R., Vroon, P.Z., 2016. Subslab mantle of African provenance infiltrating the Aegean mantle wedge. Geology 44, 367–370. https://doi.org/10.1130/g37627.1.
Klaver, M., Lewis, J., Parkinson, I.J., Elburg, M.A., Vroon, P.Z., Kelley, K.A., Elliott, T., 2020. Sr isotopes in arcs revisited: tracking slab dehydration using δ88/86Sr and 87Sr/86Sr systematics of arc lavas. Geochim. Cosmochim. Acta 288, 101–119. https://doi.org/10.1016/j.gca.2020.08.010.
Klaver, M., Matveev, S., Berndt, J., Lissenberg, C.J., Vroon, P.Z., 2017. A mineral and cumulate perspective to magma differentiation at Nisyros volcano, Aegean arc. Contributions to Mineralogy and Petrology 172. https://doi.org/10.1007/s00410-017-1414-5.
Klimm, K., Blundy, J.D., Green, T.H., 2008. Trace element partitioning and accessory phase saturation during H2O-saturated melting of basalt with implications for subduction zone chemical fluxes. J. Petrol. 49, 523–553. https://doi.org/10.1093/petrology/egn001.
Krabbenhöft, A., Eisenhauer, A., Böhm, F., Vollstaedt, H., Fietzke, J., Liebetrau, V., Augustin, N., Peucker-Ehrenbrink, B., Müller, M.N., Horn, C., Hansen, B.T., Nolte, N., Wallmann, K., 2010. Constraining the marine strontium budget with natural strontium isotope fractionations (87Sr/86Sr∗, δ88/86Sr) of carbonates, hydrothermal solutions and river waters. Geochim. Cosmochim. Acta 74, 4097–4109. https://doi.org/10.1016/j.gca.2010.04.009.
Li, H., Hermann, J., 2017. Chlorine and fluorine partitioning between apatite and sediment melt at 2.5 GPa, 800°C: A new experimentally derived thermodynamic model. 102, 580–594. 10.2138/am-2017-5891
Patino, L.C., Carr, M.J., Feigenson, M.D., 2000. Local and regional variations in Central American arc lavas controlled by variations in subducted sediment input. Contrib. Mineral. Petrol. 138, 265–283. https://doi.org/10.1007/s004100050562.
Paytan, A., Griffith, E.M., Eisenhauer, A., Hain, M.P., Wallmann, K., Ridgwell, A., 2021. A 35-million-year record of seawater stable Sr isotopes reveals a fluctuating global carbon cycle. Science (1979) 371, 1346–1350. https://doi.org/10.1126/science.aaz9266.
Pearce, C.R., Parkinson, I.J., Gaillardet, J., Charlier, B.L.A., Mokadem, F., Burton, K.W., 2015. Reassessing the stable (δ88/86Sr) and radiogenic (87Sr/86Sr) strontium isotopic composition of marine inputs. Geochim. Cosmochim. Acta 157, 125–146. https://doi.org/10.1016/j.gca.2015.02.029.
Peccia, A., Plank, T., Ding, S., Bolge, L., Aiuppa, A., Vizzini, S., Tramati, C., Taracsák, Z., Pyle, D.M., Mather, T.A., 2025. Solving the sulfur isotope discrepancy in Central America. Chem. Geol. 691. https://doi.org/10.1016/j.chemgeo.2025.122901.
Plank, T., 2014. The Chemical Composition of Subducting Sediments. In: Holland, H.D. (Ed.), Treatise on Geochemistry. pp. 607–629. https://doi.org/10.1016/B978-0-08-095975-7.00319-3.
Plank, T., Balzer, V., Carr, M., 2002. Nicaraguan volcanoes record paleoceanographic changes accompanying closure of the Panama gateway. Geology. 30. https://doi.org/10.1130/0091-7613(2002)030<1087:Nvrpca>2.0.Co;2.
Plank, T., Manning, C.E., 2019. Subducting carbon. Nature 574, 343–352. https://doi.org/10.1038/s41586-019-1643-z.
Reagan, M.K., Morris, j.D., Herrstrom, E.A., Murrell, M.T., 1994. Uranium series and beryllium isotope evidence for an extended history of subduction modification of the mantle below Nicaragua. Geochim. Cosmochim. Acta 58, 4199–4212. https://doi.org/10.1016/0016-7037(94)90273-9.
Rychert, C.A., Fischer, K.M., Abers, G.A., Plank, T., Syracuse, E., Protti, J.M., Gonzalez, V., Strauch, W., 2008. Strong along-arc variations in attenuation in the mantle wedge beneath Costa Rica and Nicaragua. Geochem., Geophys., Geosyst. 9. https://doi.org/10.1029/2008gc002040.
Révillon, S., Teagle, D.A.H., Boulvais, P., Shafer, J., Neal, C.R., 2007. Geochemical fluxes related to alteration of a subaerially exposed seamount: Nintoku seamount, ODP Leg 197, Site 1205. Geochem., Geophys., Geosyst. 8. https://doi.org/10.1029/2006gc001400.
Scher, H.D., Griffith, E.M., Buckley, W.P., 2014. Accuracy and precision of 88Sr/86Sr and 87Sr/86Sr measurements by MC-ICPMS compromised by high barium concentrations. Geochem. Geophys., Geosyst. 15, 499–508. https://doi.org/10.1002/2013gc005134.
Schettino, E., Poli, S., 2020. Hydrous carbonatitic liquids drive CO2 recycling from subducted marls and limestones. In: Manning, C.E., Lin, J.F., Mao, W.L. (Eds.), Carbon in Earth's Interior. pp. 209–221. https://doi.org/10.1002/9781119508229.ch18.
Shaw, A.M., Hilton, D.R., Fischer, T.P., Walker, J.A., Alvarado, G.E., 2003. Contrasting He–C relationships in Nicaragua and Costa Rica: insights into C cycling through subduction zones. Earth. Planet. Sci. Lett. 214, 499–513. https://doi.org/10.1016/s0012-821x(03)00401-1.
Sisson, T.W., Kelemen, P.B., 2018. Near-solidus melts of MORB + 4 wt% H2O at 0.8–2.8 GPa applied to issues of subduction magmatism and continent formation. Contrib. Mineral. Petrol. 173. https://doi.org/10.1007/s00410-018-1494-x.
Skora, S., Blundy, J., 2012. Monazite solubility in hydrous silicic melts at high pressure conditions relevant to subduction zone metamorphism. Earth. Planet. Sci. Lett. 321–322, 104–114. https://doi.org/10.1016/j.epsl.2012.01.002.
Sleep, N.H., Zahnle, K., 2001. Carbon dioxide cycling and implications for climate on ancient Earth. J. Geophys. Rese.: Planets 106, 1373–1399. https://doi.org/10.1029/2000je001247.
Solomon, E.A., Kastner, M., 2012. Progressive barite dissolution in the Costa Rica forearc – Implications for global fluxes of Ba to the volcanic arc and mantle. Geochim. Cosmochim. Acta 83, 110–124. https://doi.org/10.1016/j.gca.2011.12.021.
Spandler, C., Pirard, C., 2013. Element recycling from subducting slabs to arc crust: A review. Lithos. 170–171, 208–223. https://doi.org/10.1016/j.lithos.2013.02.016.
Spinelli, G.A., Harris, R.N., 2011. Thermal effects of hydrothermal circulation and seamount subduction: Temperatures in the Nankai Trough Seismogenic Zone Experiment transect. Japan. Geochem., Geophys., Geosyst. 12. https://doi.org/10.1029/2011gc003727. . n/a-n/a.
Syracuse, E.M., van Keken, P.E., Abers, G.A., 2010. The global range of subduction zone thermal models. Phys. Earth Planetary Interiors 183, 73–90. https://doi.org/10.1016/j.pepi.2010.02.004.
Teagle, D.A.H., Alt, J.C., Halliday, A.N., 1999. Tracing the evolution of hydrothermal fluids in the upper oceanic crust: Sr-isotopic constraints from DSDP/ODP Holes 504B and 896A. Geol. Soc., London, Special Publ. 148, 81–97. https://doi.org/10.1144/gsl.Sp.1998.148.01.06.
Turner, S.J., Barickman, M.H., Rodriguez, J., Fike, D.A., Jones, C.M., Wang, K., Savov, I.P., Agostini, S., Krawczynski, M.J., Parai, R., 2023. Boron isotopes in central American Volcanics indicate a key role for the subducting oceanic crust. Earth. Planet. Sci. Lett. 619. https://doi.org/10.1016/j.epsl.2023.118289.
Turner, S.J., Langmuir, C.H., 2022a. An evaluation of five models of Arc volcanism. J. Petrol. 63. https://doi.org/10.1093/petrology/egac010.
Turner, S.J., Langmuir, C.H., 2022b. Sediment and ocean crust both melt at subduction zones. Earth. Planet. Sci. Lett. 584. https://doi.org/10.1016/j.epsl.2022.117424.
Turner, S.J., Langmuir, C.H., 2022c. A quantitative framework for global variations in Arc geochemistry. Earth. Planet. Sci. Lett. 584. https://doi.org/10.1016/j.epsl.2022.117411.
Turner, S.J., Langmuir, C.H., 2024. An alternative to the igneous crust fluid + sediment melt paradigm for arc lava geochemistry. Sci. Adv. 10, eadg6482. https://doi.org/10.1126/sciadv.adg6482.
Turner, S.J., Langmuir, C.H., Dungan, M.A., Escrig, S., 2017. The importance of mantle wedge heterogeneity to subduction zone magmatism and the origin of EM1. Earth. Planet. Sci. Lett. 472, 216–228. https://doi.org/10.1016/j.epsl.2017.04.051.
Turner, S.J., Langmuir, C.H., Katz, R.F., Dungan, M.A., Escrig, S., 2016. Parental arc magma compositions dominantly controlled by mantle-wedge thermal structure. Nat. Geosci. 9, 772–776. https://doi.org/10.1038/ngeo2788.
van Keken, P.E., Wada, I., Abers, G.A., Hacker, B.R., Wang, K., 2018. Mafic high-pressure rocks are preferentially exhumed from warm subduction settings. Geochem., Geophys., Geosyst. 19, 2934–2961. https://doi.org/10.1029/2018gc007624.
Voigt, M., Pearce, C.R., Baldermann, A., Oelkers, E.H., 2018. Stable and radiogenic strontium isotope fractionation during hydrothermal seawater-basalt interaction. Geochim. Cosmochim. Acta 240, 131–151. https://doi.org/10.1016/j.gca.2018.08.018.
Vollstaedt, H., Eisenhauer, A., Wallmann, K., Böhm, F., Fietzke, J., Liebetrau, V., Krabbenhöft, A., Farkaš, J., Tomašových, A., Raddatz, J., Veizer, J., 2014. The Phanerozoic δ88/86Sr record of seawater: New constraints on past changes in oceanic carbonate fluxes. Geochim. Cosmochim. Acta 128, 249–265. https://doi.org/10.1016/j.gca.2013.10.006.
von Huene, R., Ranero, C.R., Weinrebe, W., Hinz, K., 2000. Quaternary convergent margin tectonics of Costa Rica, segmentation of the Cocos Plate, and Central American volcanism. Tectonics. 19, 314–334. https://doi.org/10.1029/1999tc001143.
Walker, J.A., Carr, M.J., 1986. Compositional variations caused by phenocryst sorting at Cerro Negro volcano, Nicaragua. GSA Bulletin 97, 1156–1162. https://doi.org/10.1130/0016-7606(1986)97<1156:CVCBPS>2.0.CO;2.
Watts, A., Koppers, A., Robinson, D., 2010. Seamount subduction and earthquakes. Oceanography 23, 166–173. https://doi.org/10.5670/oceanog.2010.68.
White, S.M., Crisp, J.A., Spera, F.J., 2006. Long-term volumetric eruption rates and magma budgets. Geochem., Geophys. Geosyst. 7. https://doi.org/10.1029/2005gc001002.
Workman, R.K., Hart, S.R., 2005. Major and trace element composition of the depleted MORB mantle (DMM). Earth. Planet. Sci. Lett. 231, 53–72. https://doi.org/10.1016/j.epsl.2004.12.005.
Wyllie, P., Boettcher, A., 1969. Liquidus phase relationships in the system CaO-CO2-H2O to 40 kilobars pressure with petrological applications. Am. J. Sci. 267, 489–508.
Zurek, J., Moune, S., Williams-Jones, G., Vigouroux, N., Gauthier, P.J., 2019. Melt inclusion evidence for long term steady-state volcanism at Las Sierras-Masaya volcano, Nicaragua. J. Volcanology Geothermal Res. 378, 16–28. https://doi.org/10.1016/j.jvolgeores.2019.04.007.